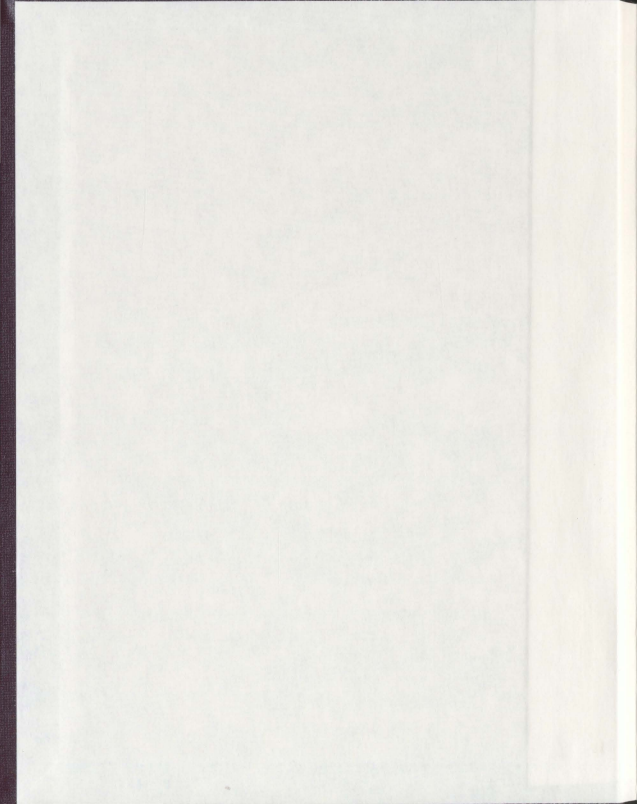


EXPERIMENTAL AND SIMULATED PROPERTIES OF  
COLLOIDALLY PATTERNED COBALT THIN FILMS

MATTHEW P. SEYMOUR







**EXPERIMENTAL AND SIMULATED PROPERTIES OF COLLOIDALLY  
PATTERNED COBALT THIN FILMS**

by:

**Matthew P. Seymour**

B. Eng. Electrical Engineering, Memorial University of Newfoundland, 2009

**A thesis submitted to the School of Graduate Studies in partial fulfillment  
of the requirements for the degree of Master of Science.**

Department of Physics and Physical Oceanography

Memorial University of Newfoundland.

December 10, 2011

ST. JOHN'S

NEWFOUNDLAND  
AND LABRADOR

## Acknowledgment

I would like to thank my supervisors Dr. Martin Plumer, Dr. Kris Poduska and Dr. Anand Yethiraj for their help and guidance. In particular, I would like to thank Dr. Yethiraj for his help with introducing me to lab work and for sharing his knowledge of colloidal science, Dr. Poduska for her help with atomic force microscopy and electrochemistry, and Dr. Plumer for his help with micromagnetism. I would also like to thank Dr. Erika Merschrod for her help with the micro patterning system and the atomic force microscope; Dr. Maynard Clouter for the use of and help with the vacuum evaporator; Dr. Liqiu Men for her help with the scanning electron microscope; and Dr. Johan van Lierop for taking hysteresis measurements of our samples.

I would like to thank the Atlantic Computational Excellence Network (ACENet) Fellowship Program for supporting my studies.

I thank my friends and family for their support during the course of my studies.

Matthew P. Seymour,            December 10, 2011.

# Contents

<b>1 Introduction</b>	<b>1</b>
1.1 Magnetic Arrays . . . . .	1
1.2 Self-Assembly and Colloids . . . . .	2
1.3 Spin-Coating and Self-Assembly . . . . .	3
1.4 Deposition of Magnetic Materials . . . . .	4
1.5 Simulations of Magnetic Materials . . . . .	5
1.5.1 Micromagnetics . . . . .	5
1.5.2 Landau-Lifshitz-Gilbert Equation . . . . .	8
1.5.3 Computation of the Equilibrium Micromagnetic Structure . . . . .	10
<b>2 Sample Preparation</b>	<b>11</b>
2.1 Substrates . . . . .	11
2.2 Spin-Coating . . . . .	12
2.3 Electrodeposition . . . . .	13
2.4 Vapour Deposition . . . . .	15
<b>3 Results and Analysis</b>	<b>17</b>
3.1 Scanning Electron Microscopy . . . . .	17

3.2	Atomic and Magnetic Force Microscopy . . . . .	18
3.3	Uses of SEM, AFM and MFM . . . . .	19
3.4	SEM, AFM and MFM Analysis . . . . .	20
3.5	Removing Spheres . . . . .	26
3.6	Magnetic Simulations . . . . .	30
3.7	Hysteresis Loop Measurements . . . . .	34
<b>4</b>	<b>Conclusions</b>	<b>38</b>
<b>A</b>	<b>Samples Prepared</b>	<b>41</b>
<b>B</b>	<b>Additional Sample Images</b>	<b>46</b>
B.1	Samples With Spheres . . . . .	46
B.1.1	Sample 168 . . . . .	46
B.1.2	Sample 172 . . . . .	56
B.1.3	Sample 173 . . . . .	65
B.1.4	Sample 174 . . . . .	68
B.2	Samples Without Spheres . . . . .	70
B.2.1	Sample 179 . . . . .	70
B.2.2	Sample 189 . . . . .	72
B.2.3	Sample 191 . . . . .	74

# List of Figures

1.1	Typical hysteresis loop showing the saturation magnetization $M_s$ , the remanent magnetization $M_r$ and the coercive field $H_c$ . . . . .	8
3.1	MFM images of a floppy disk. Recorded tracks are visible to the right of the magnetic profile. . . . .	19
3.2	SEM images of a single layer of spin-coated spheres showing domains and defects. . . . .	21
3.3	SEM images of spheres showing regions with and without electrodeposit. Sample 172: 0.5 $\mu\text{m}$ spheres spin-coated on an ITO substrate. Electrodeposit of cobalt at $-1.25$ V vs. SCE for 10 minutes. (a) shows a region that was submerged in the electrolyte during deposition, while (b) shows a region that was not. . . . .	22
3.4	SEM images of electrodeposit growth over spheres . . . . .	23
3.5	MFM images in regions with and without cobalt. Sample 172: 0.5 $\mu\text{m}$ spheres spin-coated on an ITO substrate. Electrodeposit of cobalt at $-1.25$ V vs. SCE for 10 minutes. . . . .	24
3.6	Large area MFM image. Sample 172: 0.5 $\mu\text{m}$ spheres spin-coated on an ITO substrate. Electrodeposit of cobalt at $-1.25$ V vs. SCE for 10 minutes. . . . .	25

3.7	MFM image showing cobalt deposit between spheres. Sample 182: 0.5 $\mu\text{m}$ spheres spin-coated on an ITO substrate. Electrodeposit of cobalt at $-1.25$ V <i>vs.</i> SCE; 1.499 C of charge deposited. . . . .	26
3.8	MFM image of untemplated cobalt, sample 179. Cobalt electrodeposited onto ITO substrate. $-1.25$ V <i>vs.</i> SCE; 0.999 C of charge deposited. . . .	27
3.9	MFM image of untemplated cobalt, sample 189. Cobalt electrodeposited onto ITO substrate. $-1.25$ V <i>vs.</i> SCE; 1.000 C of charge deposited. . . .	28
3.10	MFM image of untemplated cobalt, sample 191. Cobalt electrodeposited onto ITO substrate. $-1.25$ V <i>vs.</i> SCE; 1.500 C of charge deposited. . . .	29
3.11	SEM images showing cobalt deposit peeling off with spheres. The regions of bare substrate indicates that the all the material, both silica and cobalt, was removed. Sample 173: 0.5 $\mu\text{m}$ spheres spin-coated on an ITO substrate. Electrodeposit of cobalt at $-1.25$ V <i>vs.</i> SCE; 1.442 C of charge deposited. . . .	29
3.12	Hysteresis loops, various thicknesses and applied field directions, $\sigma_K = 0.05$ , $\sigma_M = 0.05$ . . . . .	31
3.13	Demagnetizing fields crossing the gaps in the magnetic template when the external field is parallel to the surface. . . . .	33
3.14	Hysteresis loops with magnetostatic interactions turned off. . . . .	35
3.15	Hysteresis loops with the exchange interaction turned off. . . . .	35
3.16	Experimentally determined hysteresis loops (Johan van Lierop, University of Manitoba) . . . . .	37
B.1	Sample 168, cobalt growth between the spheres . . . . .	47
B.2	Sample 168, cobalt growth between the spheres . . . . .	48
B.3	Sample 168, cobalt growth between the spheres . . . . .	49

B.4 Sample 168, parts of the sample where cobalt has grown over the spheres entirely . . . . .	50
B.5 Sample 168, parts of the sample where cobalt has grown over the spheres entirely . . . . .	51
B.6 Sample 168, parts of the sample where cobalt has grown over the spheres entirely . . . . .	52
B.7 Sample 168, Showing the cobalt density increasing, starting from a region which was not submerged in electrolyte during the electrodeposit, and moving towards one which was. . . . .	53
B.8 Sample 168, continuation of the series depicted in Figure B.7 . . . . .	54
B.9 Sample 168, cobalt deposit peeling off . . . . .	55
B.10 Sample 172, cobalt growth between the spheres . . . . .	56
B.11 Sample 172, cobalt growth between the spheres . . . . .	57
B.12 Sample 172, cobalt growth between the spheres . . . . .	58
B.13 Sample 172, cobalt growth between the spheres . . . . .	59
B.14 Sample 172, cobalt growth between the spheres . . . . .	60
B.15 Sample 172, cobalt growth between the spheres . . . . .	61
B.16 Sample 172, cobalt growth between the spheres . . . . .	62
B.17 Sample 172, parts of the sample where cobalt has grown over the spheres entirely . . . . .	63
B.18 Sample 172, additional MFM images depicting magnetic structure . . . . .	64
B.19 Sample 173, cobalt growth between the spheres . . . . .	65
B.20 Sample 173, cobalt growth between the spheres . . . . .	66
B.21 Sample 173, cobalt growth between the spheres . . . . .	67

B.22 Sample 174, cobalt growth between the spheres . . . . .	68
B.23 Sample 174, cobalt growth between the spheres . . . . .	69
B.24 Sample 179, additional MFM images depicting magnetic structure . . . .	71
B.25 Sample 189, additional MFM images depicting magnetic structure . . . .	72
B.26 Sample 189, additional MFM images depicting magnetic structure . . . .	73
B.27 Sample 191, additional MFM images depicting magnetic structure . . . .	74

## List of Tables

3.1	Simulated coercive fields, $\sigma_K = 0.05$ , $\sigma_M = 0.05$ . . . . .	33
3.2	Experimental coercive fields, samples 182, 183, 188 and 189 . . . . .	36
A.1	Spin coating samples. All samples made with glass slide substrate and 37 $\mu\text{L}$ of solvent. . . . .	42
A.2	Vapor deposited samples. Samples made in two batches, 64-70 and 77-84. All spin coated samples made with solvent at a concentration of 7.167 mL/g MEK to silica dropped on to a glass substrate spun at 3000 RPM. . . . .	43
A.3	Electrodeposition samples. All spin coated samples made with 37 $\mu\text{L}$ of solvent at a concentration of 7.167 mL/g MEK to silica dropped on to a substrate spun at 3000 RPM. . . . .	44
A.4	Electrodeposition samples. All spin coated samples made with 37 $\mu\text{L}$ of solvent at a concentration of 7.167 mL/g MEK to silica dropped on to a substrate spun at 3000 RPM. . . . .	45

## Abstract

Patterned magnetic films have potential uses for magnetic data storage. We develop a method to quickly manufacture patterned magnetic films using spin coating of colloidal silica spheres followed by electrodeposition of ferromagnetic cobalt. These templates have been analyzed using scanning electron microscopy and magnetic force microscopy. They possess polycrystalline ordering of the spheres, with the orientation of the crystals radial to the center of spinning. Ferromagnetic cobalt filled the interstitials between the spheres. Model structures were numerically simulated using micromagnetic software. The results of these simulations revealed differences between patterned magnetic films and uniform films. In particular, the coercive field was greater in the patterned films. On the basis of micromagnetic theory and additional simulations, we propose mechanisms to explain these differences. These results matched those reported by others who have produced patterned magnetic films. The magnetic hysteresis behaviour of several representative samples was investigated experimentally at the University of Manitoba. The results from these samples partially confirmed the behaviour seen in the simulations; however, more measurements are needed to make firm conclusions.

# Chapter 1

## Introduction

### 1.1 Magnetic Arrays

Hard disks used for storage in modern computers record information by writing bits on a magnetic thin film. This film is granular and has its crystalline anisotropy axis perpendicular to the plane of the film.<sup>1</sup> In order to achieve greater data densities it is necessary to decrease the area used per bit. Each recorded bit is composed of many magnetic single domain grains, and in order to decrease the area covered by a single bit while maintaining a good signal-to-noise ratio, it is necessary to keep the number of grains per bit approximately constant by decreasing the grain size of the films.<sup>2</sup> In order to prevent long term signal decay by thermal activation, the magnetic anisotropy  $K$  must then increase as the grain size  $V$  decreases since the energy barrier to magnetic domain flipping is  $E_B = KV$ .<sup>1</sup> Eventually, the inability of the recording head field to reverse grains having such large anisotropy will limit the recording density.<sup>1</sup>

Several solutions to the problem of increasing data density have been discussed. One option is to use Heat Assisted Magnetic Recording (HAMR),<sup>3</sup> a technique that uses laser

heat to overcome the large anisotropy required for higher densities. The bit is heated and then cooled in the presence of the writing field. This serves to temporarily reduce the effective anisotropy. Another solution is to isolate each magnetic bit as a single grain. The current approach requires many grains ( $N$  per bit) in order to average the anisotropy, position and magnetization fluctuations over the grains. This gives a statistical signal to noise ratio proportional to  $\sqrt{N}$ . However, when each bit is a single grain this is not required, and therefore a magnetic array can use larger grain sizes than the equivalent density traditional media.<sup>1,4</sup> This approach is referred to as bit patterned media, and it is the focus of this thesis.

## 1.2 Self-Assembly and Colloids

One method used to create magnetic arrays is to start with a template, and then deposit magnetic material around the template.<sup>5</sup> The template can then be removed or left in place if it does not interfere magnetically. The result is a patterned array of magnetic material.

This template can be produced using photolithography, but a different technique is to use the process of self-assembly instead. Self-assembling systems spontaneously arrange their components into large periodic structures. Using self-assembly can greatly reduce the cost and complication of producing templates. In contrast with photolithography, which is a challenge to scale down,<sup>6</sup> self-assembly can in principal be extended well into the nanoscale. For this thesis, we use the self-assembly of colloidal silica spheres to create our template.

A colloidal system is a heterogeneous system in which small particles or droplets (the *dispersed* phase) are suspended in a continuous medium (the *continuous* phase), usually

a liquid. The particles or droplets are usually of order  $10\ \mu\text{m}$  or less.<sup>7</sup> Either phase can be solid, liquid or gas, although they cannot both be gaseous. Common everyday examples include milk (fat globules dispersed in water), smoke (particles dispersed in air), and fog (liquid droplets dispersed in air). This project uses solid silica spheres dispersed in a liquid. These systems show many interesting properties. The colloidal spheres undergo Brownian motion, and experience forces such as electrostatic and Van der Waals.<sup>7</sup> Additionally, as particles move through the fluid they displace it, and this displacement affects the motion of nearby particles. These interactions are called hydrodynamic interactions.<sup>8</sup>

### 1.3 Spin-Coating and Self-Assembly

To create templates using self-assembly, we spin-coat colloidal silica spheres with diameters of either  $0.25\ \mu\text{m}$  or  $0.5\ \mu\text{m}$  dispersed in a solvent. The substrate is set to spin at a high speed (several thousand revolutions per minute), and a small amount of the solution is dropped onto the spinning substrate. As the solvent evaporates, the solid silica spheres self-organize into many small crystal domains on the substrate.

When colloidal spheres are organized into a periodic array, they influence the propagation of light in interesting ways. Light waves that are not equal in wavelength to the periodicity of the array will be attenuated while those that match the periodicity are not, in a process similar to x-ray diffraction in atomic crystals, namely, Bragg diffraction.<sup>5,9</sup> In Bragg diffraction, the attenuation of a particular wavelength is dependent on the angle between the source and the observer. Therefore the wavelengths, and thus the colors, of the light that is seen will change based on viewing angle. This phenomenon accounts for the striking iridescent colours of natural opals.<sup>5,9</sup>

Where the sample consists of a single crystal domain, one would expect to see a

single colour, that would change based on viewing angle (neglecting the differences in angle due to perspective). This is not observed. Instead, a strong radial pattern is seen when viewing the samples made *via* spin-coating.<sup>10-12</sup> This suggests that the resulting sample is polycrystalline, with the individual grains oriented radially from the center of spinning.<sup>11,12</sup> This has been confirmed by both scanning electron microscopy (SEM) and atomic force microscopy (AFM).<sup>12</sup>

## 1.4 Deposition of Magnetic Materials

Once a template is formed, magnetic material must be laid down. For the purposes of magnetic storage, a ferromagnetic material is used, since they retain their magnetization after the magnetic field has been removed.<sup>13</sup> For this project, cobalt was chosen. Cobalt has a high magnetic anisotropy,<sup>14</sup> and thus a larger energy barrier, which helps keep the magnetization pointing in one direction, an important feature for the stability of magnetic storage. Cobalt also has the advantage of being a relatively cheap magnetic material compared to rare earth elements. It is also significantly easier to deposit single elemental materials as opposed to alloys.

In this thesis work two techniques were used to deposit cobalt. The first is electrodeposition. For electrodeposition, an electrically conductive substrate is used, and the template is submerged in an electrolyte containing  $\text{CoSO}_4$ . When a negative potential is applied between the substrate and a reference electrode the cobalt deposits on the surface, filling in the areas around the template.

The second technique used is vapour deposition. Here the substrate need not be electrically conductive. The substrate and a filament containing cobalt pellets are placed in a vacuum chamber. Once the air is evacuated, the filament is heated up by running current

through it, and this causes the cobalt to evaporate and deposit onto the surface of the substrate.

There are several reasons for investigating these two different techniques. They both have advantages and disadvantages. Electrodeposition can take place without the need for a vacuum, is more easily controlled, and allows for thicker deposits. Vapour deposition does not require a conducting substrate. There is also a fundamental difference between these two techniques: while in electrodeposition the deposit grows from the substrate upwards, filling in around the template, in vapour deposition the deposit is from above and is laid down on both substrate and template. Both types of deposits are potentially interesting to investigate.

## 1.5 Simulations of Magnetic Materials

One of the major goals of this thesis is to compare experimental results with simulations of the magnetic arrays. To perform these simulations, the commercial software package *LLG Micromagnetics*<sup>15</sup> is used. This software is based on the Landau-Lifshitz-Gilbert equation.<sup>16</sup>

### 1.5.1 Micromagnetics

The magnetic structure of a solid is ultimately based on the configuration of the individual magnetic moments of the atoms that compose it. These individual moments are too numerous to simulate directly, however. Micromagnetics takes a continuum limit of the magnetic moments, defining the *magnetization* as:<sup>17</sup>

$$\mathbf{M}(\mathbf{r}) = \frac{\sum \boldsymbol{\mu}_j}{dV_{\mathbf{r}}} \quad (1.1)$$

where  $\mu_j$  are the individual atomic magnetic moments, and  $dV_r$  represents a volume large enough to contain many moments, but small enough that we can treat  $\mathbf{M}$  as continuous.

The arrangement of magnetic moments, and therefore the magnetization, is the result of the competition of several interactions.

The *exchange interaction* is a short range interaction between magnetic moments.<sup>13</sup> The interaction is a quantum mechanical effect. It arises due to the requirements of the Pauli exclusion principle, which in its most general form states that the wavefunction of several particles must be either symmetric for bosons or antisymmetric for fermions (like electrons) under the exchange of two particles (this is where the name "exchange interaction" comes from). In ferromagnets the exchange interaction causes nearby magnetic moments to align. Energetically, it penalizes any non-uniform arrangement of the magnetization. As a result, the exchange interaction causes long range order in ferromagnets. The atomic moments of large regions of the magnet will point in the same direction. These regions are referred to as magnetic domains. The boundaries between magnetic domains are called domain walls. The exchange interaction ensures that these walls do not exhibit discontinuous jumps in magnetization but rather change gradually from one direction to another.

Domain walls have an energy cost, and if exchange were the only interaction at play these gradually changing domain walls would simply unwind themselves until they reached through the entire system.<sup>13</sup> However there is another interaction at play - *magnetocrystalline anisotropy*. Crystals of magnetic materials possess an easy axis and a hard axis, which are related to their crystal symmetry. It is more energetically favourable for the magnetization to point along either direction of the easy axis than elsewhere. Thus a domain wall is a balance between the anisotropy energy which tends to keep the mag-

netization aligned to the easy axis and the exchange interaction which tends to favour a smooth variation in the magnetization.

Why are there different domains in the first place? Firstly, in a polycrystalline material, the different crystal domains will each have their own easy axis and therefore the magnetization will tend to point along different directions in different crystal domains. Secondly, domain formation saves energy associated with the *magnetostatic interaction*. For well separated magnetic moments, the magnetostatic interaction reduces to the simple dipole-dipole interaction. If an entire sample is magnetized along one direction this produces an external *demagnetizing field*, which costs energy. Therefore, it is energetically favourable to have the magnetization pointing parallel to the material's surface. This results in the creation of domains as the magnetization tries to avoid pointing out of any of the sample's surfaces. The domain structure of the sample is a result of the competition of these three interactions: exchange, anisotropy, and magnetostatic.<sup>13,18</sup>

When an external magnetic field  $\mathbf{H}$  is applied, a fourth interaction (the Zeeman term,  $-\mathbf{M} \cdot \mathbf{H}$ ) comes into play, causing the magnetization to try to point along the same direction as  $\mathbf{H}$ . The easiest way for the magnetization to align itself with the external field is by domain wall motion. Domain walls move so as to increase the size of domains which are aligned (or partially aligned) to the external field, while shrinking those which are not.<sup>13</sup> At higher fields, domains will rotate to the easy axis nearest that of the external field. And lastly, at very high fields, the domains will start to move from the direction of the easy axis to that of the field, with the energy savings of pointing along the field being greater than the costs of not pointing with the easy axis. When all the magnetic moments point the same way, the sample is at its saturation magnetization,  $M_s$ .

When the external field is removed, some magnetization remains; to get back to zero

net magnetization would require domain rotations or domain wall movements. This zero field magnetization is called the remanent magnetization,  $M_r$ . To force the sample back to zero magnetization requires the application of an external field pointing in the opposite direction, the strength of which is known as the coercive field,  $H_c$ . Therefore, the magnetization of a sample depends not only on the external field, but also on the history of that field. This property is known as hysteresis. By plotting the magnetization against the external field as the magnetization is brought from saturation in one direction to the other and back again, one obtains a hysteresis loop. A typical hysteresis loop can be seen in Figure 1.1. Hysteresis loops are obtained from magnetic simulations, or experimentally from a magnetometer. Magnetic domains near the surface can be visualized by magnetic force microscopy.<sup>19</sup>

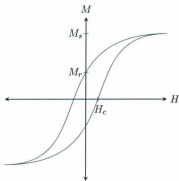


Figure 1.1: Typical hysteresis loop showing the saturation magnetization  $M_s$ , the remanent magnetization  $M_r$ , and the coercive field  $H_c$ .

### 1.5.2 Landau-Lifshitz-Gilbert Equation

The magnetization is a function of time as well as position. In the presence of a magnetic field, the magnetization vector will precess with a frequency determined by the torque

equation:<sup>18,20</sup>

$$\frac{\partial \mathbf{M}}{\partial t} = -\gamma \mathbf{M} \times \mathbf{H} \quad (1.2)$$

where  $\gamma$  is the gyromagnetic ratio. Here  $\mathbf{H}$  is the magnetic field. The magnetization is affected by more than just external fields, however. In addition to external fields, the magnetization is affected by the exchange interaction, anisotropy, magnetostatic dipole interactions with the rest of the magnetic structure, and demagnetizing fields.<sup>21</sup> However, we can represent these effects with an *effective field*,  $\mathbf{H}_{\text{eff}}$ :

$$\frac{\partial \mathbf{M}}{\partial t} = -\gamma \mathbf{M} \times \mathbf{H}_{\text{eff}}. \quad (1.3)$$

This model would have the magnetization precessing endlessly about the effective field. In real systems, damping due to various dissipative effects causes the magnetization vector to settle down and point along the direction of the effective field. Landau and Lifshitz represented this damping by an additional torque term which rotates the magnetization towards the effective field.<sup>22,17</sup>

$$\frac{\partial \mathbf{M}}{\partial t} = -\gamma \mathbf{M} \times \mathbf{H}_{\text{eff}} - \frac{\gamma \alpha}{M_s} \mathbf{M} \times (\mathbf{M} \times \mathbf{H}_{\text{eff}}) \quad (1.4)$$

where  $\alpha$  is a phenomenological parameter known as the damping parameter, and  $M_s$  is the saturation magnetization. Gilbert took a different approach. He introduced damping by adding a kind of viscous force, given by:<sup>17</sup>

$$\frac{\alpha}{M_s} \mathbf{M} \times \frac{\partial \mathbf{M}}{\partial t} \quad (1.5)$$

to Equation 1.3. After some manipulation, the resulting equation becomes:

$$\frac{\partial \mathbf{M}}{\partial t} = -\frac{\gamma}{1 + \alpha^2} \mathbf{M} \times \mathbf{H}_{\text{eff}} - \frac{\gamma \alpha}{(1 + \alpha^2) M_s} \mathbf{M} \times (\mathbf{M} \times \mathbf{H}_{\text{eff}}) \quad (1.6)$$

known as the Landau-Lifshitz-Gilbert (LLG) equation.<sup>20</sup> Notice that Equations 1.4 and 1.6 are equivalent in the limit of vanishing  $\alpha$ . Both equations yield similar results.

### 1.5.3 Computation of the Equilibrium Micromagnetic Structure

Simulations are performed by first discretizing the film into a set of magnetic cells, each having a uniform magnetization vector  $\mathbf{M}_i$ . The LLG equation is then solved for each cell numerically, with  $\mathbf{H}_{\text{eff}}$  accounting for their interactions, until they have reached equilibrium. When trying to find the equilibrium magnetization structure numerically, it is not necessary to solve Equation 1.6 directly. Instead, note that, at equilibrium,  $\partial \mathbf{M} / \partial t = 0$ . This means that we can find the micromagnetic structure by iteratively relaxing the magnetization vector along the direction of the effective field.<sup>16</sup> The residual is then computed as:

$$\frac{\mathbf{M}_i \times \mathbf{H}}{M_i H} = \frac{M_i H \sin(\theta)}{M_i H} \mathbf{n} = \sin(\theta) \mathbf{n} \quad (1.7)$$

where  $\mathbf{n}$  is a unit vector perpendicular to  $\mathbf{M}_i$  and  $\mathbf{H}$ , and  $\theta$  is the angle between them. The residual is therefore a measurement of the alignment between  $\mathbf{M}_i$  and  $\mathbf{H}$ . When the cell with the largest residual is less than the convergence minimum, the iteration process is stopped.<sup>16</sup> The convergence minimum is set small enough that the structure can be considered to approximately be in equilibrium. It is this process that is used by the *LLG Micromagnetics* software.<sup>16</sup> LLG simulations can be used to model hysteresis loops.

## Chapter 2

# Sample Preparation

There are several steps involved in making the magnetic patterns. First, the substrate is prepared and cleaned. Then colloidal spheres are spin-coated onto the substrate to create the template for the pattern. This is followed by either electrodeposition or vapour deposition to create the magnetic pattern. Attempts have been made to remove the spheres after the deposition step, however a reliable method has not been found so far. A summary of the samples made is given in Appendix A.

### 2.1 Substrates

Selection of the substrate is based on several considerations. If the sample is to be made using electrodeposition, then the substrate must be conducting. The substrate must not be magnetic so that it will not interfere with the magnetic array. The substrate must be clean and smooth for the spin-coating process, and the silica spheres must adhere well enough to the substrate to remain during cleaning and deposition. However, removability of the spheres is also a useful property once the magnetic material has been deposited.

Keeping the substrate clean is important at each stage of the sample preparation

process. This is usually accomplished by rinsing with ethanol followed by ultrapure (18.2 M $\Omega$  · cm) water. Compressed air is used to remove dust.

For samples made using electrodeposition, indium tin oxide (ITO) coated glass was used as the substrate. This clear, conducting material provides a smooth surface to spin-coat and electrodeposit upon. ITO coated cover slides (20 × 20 mm, SPI Supplies) were glued to glass microscope slides using an ultraviolet light activated adhesive (Norland UV Sealant 91) to assist with spin-coating. Later samples used ITO coated glass slides (25 × 25 mm, Delta Technologies), which obviated the need to glue them to microscope slides. For samples made using vapour deposition, 3" × 1" glass microscope slide (Fisher-brand Microscope Slides) substrates were used.

## 2.2 Spin-Coating

Before spin-coating a colloidal suspension must be prepared. The thickness (in layers of spheres) of the spin-coated sediment is determined by the physical parameters of the suspension (such as viscosity, vapour pressure, and colloid volume fractions) and the spin-coating parameters. In order to produce a single layer, silica spheres either 0.25  $\mu\text{m}$  or 0.50  $\mu\text{m}$  in diameter (Fiber Optic Center Inc. AngstromSphere) were mixed with methyl ethyl ketone (MEK), or 2-Butanone, at a ratio of 7.167 mL of MEK for each gram of silica. With a density of 0.805 g/cm<sup>3</sup> at room temperature this gives a mass fraction of 5.769 MEK to silica. The spheres were dried for three or more hours in an oven at 150°C to remove absorbed water prior to preparation of the suspension. In order to disperse the spheres evenly, the suspension was ultrasonicated for several hours prior to spin-coating. The resulting suspension is milky white due to scattering by the dispersed spheres.

The substrate was spun at 3000 RPM and 37  $\mu\text{L}$  of the colloidal suspension was

dropped at the center of rotation using a pipettor. Within seconds, the MEK evaporates leaving the spheres behind. This procedure generated a single layer of spheres for both 0.25  $\mu\text{m}$  and 0.50  $\mu\text{m}$  sphere diameters. Decreasing the ratio of MEK to silica, or lowering the spinning speed, can result in more layers.

### 2.3 Electrodeposition

For electrodeposition, an electrolyte of 0.1M  $\text{H}_3\text{BO}_3$  (boric acid, EM Science, 99.5% pure), 0.1M  $\text{CoSO}_4$  (cobalt sulfate, EM Science, 97.0% pure) was prepared. Cobalt sulfate and boric acid are commonly used for cobalt electrodeposits.<sup>23-27</sup> The boric acid acts as a buffer to stabilize the pH during the deposit. A three electrode system was used with a counter electrode, working electrode and reference electrode. The potential of the working electrode with respect to the reference electrode is kept at a constant value, while electrochemical reactions occur at the working and counter electrodes. In our cell, the following reactions take place:<sup>28</sup>

Counter Electrode:



Working Electrode:



The working electrode is the substrate (ITO) upon which the cobalt is deposited. The

connection to the substrate was made directly with a toothless alligator clip. Gold was used for the counter electrode, and the reference electrode was saturated calomel (SCE). The half-cell reaction in Equation 2.2 has a potential of  $-0.277$  V *vs.* the standard hydrogen electrode (SHE),<sup>28</sup> or  $-0.519$  V *vs.* SCE. Taking into account the concentration of  $\text{Co}^{2+}$ ,  $0.1\text{M}$ , the Nernst potential at room temperature is  $-0.490$  V.

The cobalt was deposited with a constant applied potential using a Hokuto Denko HA 501 potentiostat/galvanostat. The two most important parameters during the electrodeposition step are the electrode potential and the deposition time. Values between  $-1.1$  V to  $-1.25$  V *vs.* saturated calomel were tried, for times up to 10 minutes. We can estimate the average thickness of the deposit knowing the amount of charge  $Q$ , the density of cobalt  $\rho$ , the atomic mass of cobalt  $m$ , the surface area  $A$  and the charge donated to each cobalt atom  $q$ . The thickness  $T$  can be calculated as:

$$T = \frac{Qm}{q\rho A}. \quad (2.4)$$

In the present case each cobalt atom receives two electrons ( $q = -2e$ ).  $Q$  itself is found by integrating the current over the time of the deposit. Since the current is nearly constant during the deposit step, the charge can be approximated as the product of current and deposit time,  $Q = It$ . For later samples, the charge was measured directly. Of course, in reality, a fraction of the surface area is blocked by the template and this means the resulting pattern will be thicker. On the other hand, a significant portion of the charge will have been used to evolve hydrogen gas (Equation 2.3) and this means the deposit will be thinner than calculated. Note also that the current efficiency can be altered when depositing in confined spaces,<sup>29</sup> which could affect deposits on templated samples.

The electrodeposition step is strongly dependent on how clean the substrate and solution are. Impurities can lead to uneven covering of the substrate. The electrolyte is not used for more than three deposits before replacement.

## 2.4 Vapour Deposition

Vapour deposition is done *via* thermal evaporation of the deposited material onto the surface of the target under vacuum. The cobalt pellets (Kurt J. Lesker Company, 99.95% pure) are placed in a tungsten basket (Kurt J. Lesker Company, EVSME16A030W), while the sample is held in place by a bracket facing downwards. The air is pumped out of the chamber, first using a roughing pump, and then using a diffusion pump. Current is then passed through the basket, heating it up. The cobalt evaporates from the surface and is deposited on the sample. For vapour deposition, Maynard Clouter's custom made system was used.

The vapour deposition chamber has two circuits available. This allows for two baskets to be operated independently. If it is desirable to prevent oxidation of the film prior to removing the vacuum, then a copper film can be evaporated using the second circuit on top of the cobalt film in order to seal it (copper shot, Central Scientific Company (CENCO)). Alternatively, cobalt can be placed in both baskets in order to obtain a thicker film.

Several challenges presented themselves during the vapour deposition. Cobalt tends to alloy with refractory metals such as the tungsten filament, and this weakens the filament. In addition, the temperature of the filament is controlled manually by changing the current through it. Since there is no temperature sensor, this means that control of the temperature of the filament is at best crude. Given this and the relatively high melting

point (1768 K) of cobalt,<sup>30</sup> breaks of the filament were common. The filament breaking before all the metal evaporates results in thin deposits and a lack of control over the deposit thickness.

Deposit thickness can be estimated by taking the mass of metal to be deposited  $m$ , its density  $\rho$ , and the distance at which the substrate is held from the basket during deposition  $r$ . Also required is the angular dependence of the evaporation — it is not uniform in all directions, since it is blocked by the filament. As an approximation, assume that the evaporation is spread evenly across one hemisphere. Then the thickness of the deposit can be estimated as:

$$T = \frac{m}{2\pi r^2 \rho} \quad (2.5)$$

Using some typical values for a deposit:

$$T = \frac{(0.5 \text{ g})}{2\pi(50 \text{ cm})^2(8.9 \text{ g/cm}^3)} \approx 36 \text{ nm} \quad (2.6)$$

This assumes that all the metal is evaporated. As mentioned above though breaks of the basket were frequent, and this results in thinner deposits.

## Chapter 3

# Results and Analysis

### 3.1 Scanning Electron Microscopy

Scanning Electron Microscopy (SEM) uses a beam of electrons to investigate the surface of a sample. A high energy beam of electrons (for this thesis, 15 keV) is focused on the surface using magnetic lenses. Upon interaction with the surface, this beam produces backscattered electrons (reflected from the original beam), secondary electrons (knocked loose from the sample) and x-rays (due to electrons dropping down into the empty orbitals of displaced electrons).

Due to the shorter wavelength of high energy electrons as compared to visible light, SEM can achieve greater resolution than optical microscopy. This makes it useful for investigating colloidal spheres that are on the order of (or smaller than) the wavelength of visible light. However SEM cannot give quantitative height measurements.

In order to avoid charging due to the electron beam, the sample must be conductive. If it is not intrinsically conductive, it must be coated with a thin layer of conductive material, usually gold. For our samples on ITO, this step was not necessary.

### 3.2 Atomic and Magnetic Force Microscopy

Atomic Force Microscopy (AFM) uses a small cantilever to scan the surface of the sample. There are two modes that AFM uses: contact mode and tapping (or AC) mode. In contact mode, the cantilever is pressed into contact in the surface. A laser reflecting off the back of the cantilever is used to measure its deflection and a feedback mechanism keeps this deflection constant by moving the sensing head up and down with respect to the sample. As the cantilever is scanned across the surface, the output of this feedback mechanism is recorded to obtain the height profile of the surface. This allows the AFM to obtain quantitative height profiles. In AC mode, the cantilever is mechanically driven in one of its resonant modes, and the amplitude is recorded. The presence of a nearby surface reduces the amplitude, and feedback is used to keep the amplitude constant while scanning, in a manner similar to contact mode. In addition to the amplitude, the phase (relative to the driver) is also recorded.

This phase information is used in Magnetic Force Microscopy (MFM). MFM uses a magnetized cantilever tip. The process is similar to AFM, except that each line is scanned twice. On the second pass the cantilever tip is kept at a predetermined height above the surface (as recorded on the first pass). This height level is chosen such that interactions from the surface itself are minimal. At this distance, the magnetic forces on the cantilever alter the phase of its oscillations, and the recordings of the phase difference show magnetic features of the sample. Specifically, MFM is a measure of the second spatial derivative of the sample's magnetic field.<sup>31</sup> Figure 3.1 shows a comparison of the height and magnetic profiles of a magnetic storage floppy disk taken with MFM.

Normally when doing AFM, and not MFM, gold-coated silicon cantilevers are used. When doing MFM, the cantilever tip must be magnetic, and silicon cantilevers coated in

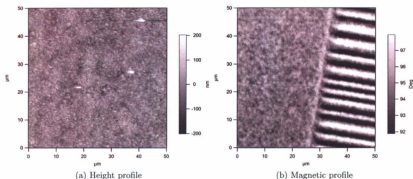


Figure 3.1: MFM images of a floppy disk. Recorded tracks are visible to the right of the magnetic profile.

a layer of cobalt and a second layer of chromium (to prevent oxidation of the cobalt) are used. In the past, other students in our group have found it difficult to image spin-coated colloidal silica spheres with AFM, due to the tip moving or dragging the spheres out of place. However during the course of this project it was found that the chrome-cobalt coated cantilevers did not significantly disrupt the spheres when used in AC mode, and were therefore suitable for taking height profiles of colloids, in addition to magnetic measurements.

### 3.3 Uses of SEM, AFM and MFM

The ultimate goal of this thesis is to compare magnetic templates produced in the laboratory with computer simulations. SEM and AFM play important roles in this goal. The use of SEM and MFM have been invaluable in refining the experimental procedure used to produce these samples. A combination of SEM and AFM measurements were used to determine how many layers of spheres were laid down by the spin-coat process, which allowed for the refinement of the spin-coating parameters (rotation rate, initial colloid vol-

ume fraction) to produce the desired number of layers (in our case, one layer was desired, although we did produce some two and three layer samples). SEM and MFM measurements were also used to refine the electrodeposition time to obtain cobalt films of the desired thickness. AFM and SEM were used to evaluate the effectiveness of techniques to remove spheres (see Section 3.5). SEM and MFM are also valuable for identifying candidate samples to take further measurements on (see Section 3.7).

In addition to these experimental uses, MFM and SEM provide information about the samples relevant to simulations. SEM provides information on the symmetry and general structure of the sphere placement. This can be important in determining where and how far apart to place voids in simulations. AFM reveals that the cobalt film is polycrystalline and allows a determination of the size of the crystal grains (see Section 3.4). As crystal structure plays a vital role in micromagnetics (due to crystalline anisotropy), this information is important in creating representative simulations. MFM gives similar information regarding the size of magnetic domains.

### 3.4 SEM, AFM and MFM Analysis

Samples (see Appendix A) were examined with an Hitachi S-570 SEM and an Asylum Research MFP-3D-SA AFM/MFM. Two different cantilever tips were used. For initial AFM experiments, MikroMasch Ultrasharp silicon cantilevers with a chromium/gold coating (CSC37/Cr-Au) were used. However, they move the spheres during imaging. For later magnetic imaging, MikroMasch Ultrasharp silicon cantilevers with a cobalt/chromium coating (NSC36/Co-Cr) were used. These tips were capable of imaging the colloidal particles without moving them, in addition to their suitability for magnetic imaging. All images presented in this chapter were taken with this kind of tip. Under the conditions

used, spin-coated single layers of spheres consistently produced a polycrystalline close packed structure. Crystal domains are small – usually no more than a few dozen spheres, although the size of the domains increases with distance from the center of spinning<sup>32</sup> – and defects are common. Typical examples are shown in Figure 3.2.

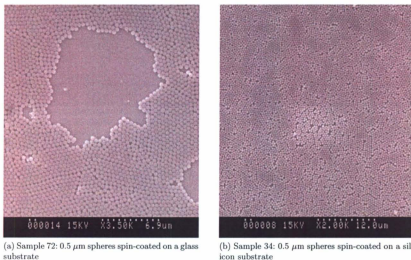


Figure 3.2: SEM images of a single layer of spin-coated spheres showing domains and defects.

Although removing the spheres without removing the deposit proved difficult, it was possible to examine the samples with the spheres in place. With deposits of sufficient thickness, the electrodeposited cobalt was visible between the spheres under SEM. Although the colours seen with SEM are not quantitative (since they depend on both topography and composition of the sample), we can compare regions submerged in the electrolyte with those which were not. For example, in Figure 3.3 (a), the presence of cobalt is indicated by the lightly coloured regions surrounding the spheres. This light colouring is absent in regions that were not submerged in the electrolyte during deposition, as shown in Figure 3.3 (b). When scanned with MFM (see below), magnetic signals

were found in areas as shown in Figure 3.3 (a) while no magnetic signal was found in areas like those in (b). When the thickness of the deposit is even greater, it rises above the spheres, as can be seen in Figures 3.4 (a) and (b).

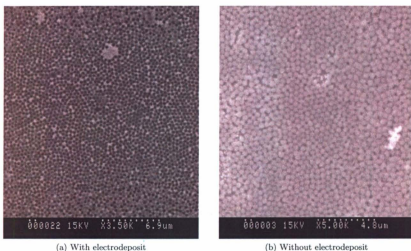
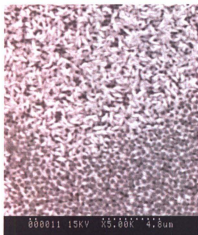


Figure 3.3: SEM images of spheres showing regions with and without electrodeposit. Sample 172:  $0.5 \mu\text{m}$  spheres spin-coated on an ITO substrate. Electrodeposit of cobalt at  $-1.25 \text{ V vs. SCE}$  for 10 minutes. (a) shows a region that was submerged in the electrolyte during deposition, while (b) shows a region that was not.

When examined with MFM, the electrodeposit between the spheres does not always appear in the height profile, unless there is a large gap or the deposit has grown over the spheres. However, comparisons of magnetic profiles in regions containing deposits against those without demonstrate the presence of the magnetic material. Figure 3.5 shows the contrast. Notice how the magnetic profile in the region without cobalt only shows background noise, while the magnetic profile in the region with cobalt reveals magnetic structure. Locations where spheres are still present appear darker because the cantilever tip is effectively much further from the underlying magnetic material than it is between the spheres. This is because the retrace uses the height profile as its reference



(a) Sample 172: 0.5  $\mu\text{m}$  spheres spin-coated on an ITO substrate. Electrodeposit of cobalt at  $-1.25$  V vs. SCE for 10 minutes.



(b) Sample 168: 0.5  $\mu\text{m}$  spheres spin-coated on an ITO substrate. Electrodeposit of cobalt at  $-1.25$  V vs. SCE for 10 minutes.

Figure 3.4: SEM images of electrodeposit growth over spheres

point, which includes the spheres. Larger area images are needed to show details of larger magnetic structures. Figure 3.6 shows a larger area scan of the sample in Figure 3.5.

Rarely, large enough gaps occurred between the spheres to image the cobalt between them. Figure 3.7 shows one such image.

Untemplated samples were also made and imaged for comparison. Figure 3.8 shows small and large area images of one such sample, while Figure 3.9 shows scans from another sample. Both of these deposits are approximately the same thickness: each deposit had 1 C of charge deposited (with an area of  $2.5 \text{ cm}^2$ , Equation 2.4 gives a thickness of about 140 nm). Figure 3.10 shows a sample with a thicker film, with 1.5 C deposited. It can be seen from these images that magnetic domain structure appears to be correlated with crystal domain structure, this being expected from crystal induced anisotropy. If the points in the height profile are labeled  $x_i$ , and the corresponding points in the magnetic

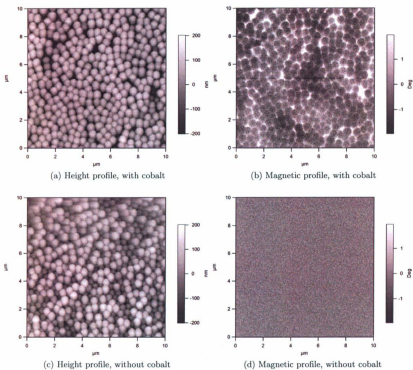


Figure 3.5: MFM images in regions with and without cobalt. Sample 172:  $0.5 \mu\text{m}$  spheres spin-coated on an ITO substrate. Electrodeposit of cobalt at  $-1.25 \text{ V vs. SCE}$  for 10 minutes.

profile are labeled  $y_i$  then the sample correlation coefficient  $r$  can be written as

$$r = \frac{\sum_{i=1}^n (x_i - \bar{x})(y_i - \bar{y})}{\sqrt{\sum_{i=1}^n (x_i - \bar{x})^2} \sqrt{\sum_{i=1}^n (y_i - \bar{y})^2}} \quad (3.1)$$

where  $\bar{x}$  and  $\bar{y}$  are the respective means.  $r$  lies in the range  $[-1, 1]$ , with  $r = \pm 1$  corresponding to a perfectly linear relationship and  $r = 0$  to no relationship. For Figures 3.8 (a) and (b)  $r = -0.1829$ ; for Figures 3.8 (c) and (d)  $r = -0.1961$ ; for Figures 3.9 (a) and (b)  $r = -0.3099$ ; and for Figures 3.9 (c) and (d)  $r = -0.3977$ . These correlations are

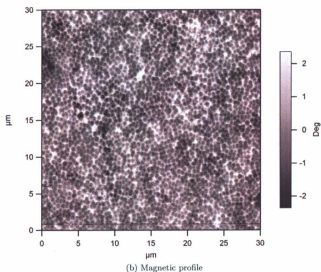
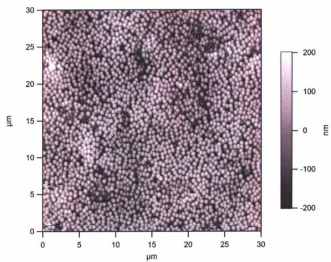


Figure 3.6: Large area MFM image. Sample 172:  $0.5 \mu\text{m}$  spheres spin-coated on an ITO substrate. Electrodeposit of cobalt at  $-1.25 \text{ V vs. SCE}$  for 10 minutes.

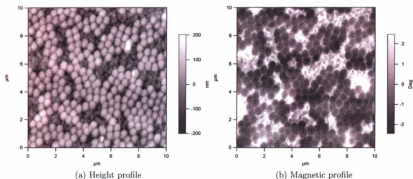


Figure 3.7: MFM image showing cobalt deposit between spheres. Sample 182:  $0.5 \mu\text{m}$  spheres spin-coated on an ITO substrate. Electrodeposit of cobalt at  $-1.25 \text{ V vs. SCE}$ ;  $1.499 \text{ C}$  of charge deposited.

rather weak. This could be due to a non-linear relationship, or it could be that the images agree on the edges of the crystal/magnetic domains, but possess little correlation otherwise. While these correlations appear to be weak, they do not appear to be insignificant: comparisons of unrelated images give much smaller  $r$  values. For example, for Figures 3.8 (a) and (d)  $r = -0.0197$ ; while for Figures 3.8 (c) and (b)  $r = 0.00107$ .

### 3.5 Removing Spheres

As described above, in MFM the cantilever makes a second pass using the height profile of the first pass as its guide in order to record information about the magnetic structure of the sample. Ideally the tip will be kept at a constant height above the surface of the magnetic material during this pass so that the structure seen in the image can be correlated to the actual magnetic structure in the sample. Unfortunately, with the spheres still in place, the distance between the tip and the magnetic material beneath the spheres is no longer held constant. It will be at a maximum when the tip is over the center of the

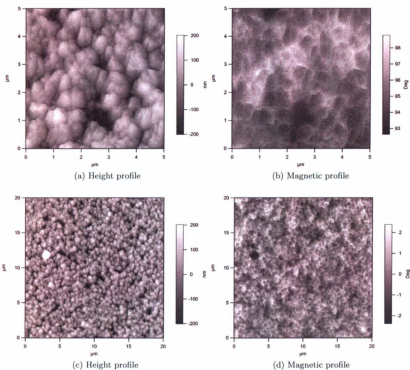


Figure 3.8: MFM image of untemplated cobalt, sample 179. Cobalt electrodeposited onto ITO substrate.  $-1.25$  V vs. SCE;  $0.999$  C of charge deposited.

sphere and at a minimum when between the spheres, the difference being the sphere's diameter (500 nm in the case of the larger spheres or 250 nm for the smaller ones). Since the fly height used is 200 nm, this is clearly significant, and the effect can be seen in the images in the previous section.

With this in mind, attempts were made at removing the spheres while leaving the cobalt deposit intact. These attempts were met with little success. The cobalt layer, especially the more desirable thicker deposits (1 C or more of charge deposited), washes off easily in water. Figure 3.11 shows how the cobalt deposit peeled off with the spheres

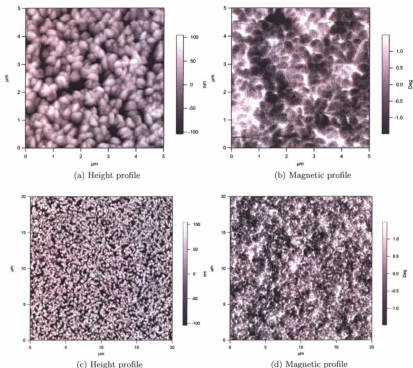


Figure 3.9: MFM image of untemplated cobalt, sample 189. Cobalt electrodeposited onto ITO substrate.  $-1.25$  V vs. SCE;  $1.000$  C of charge deposited.

in one sample, in this case as a result of washing the sample in water after depositing it.

While thicker deposits would wash off in water, the thinner were more robust, and so attempts were made to remove the spheres while keeping the cobalt. Several of the techniques tried to remove the spheres include: dipping the sample in water and letting it dry; dipping the sample in MEK and letting it dry; dipping the sample in  $H_2SO_4$  and washing it in water; ultrasonically cleaning the sample in water; ultrasonically cleaning the sample in NaOH; wiping the sample with a cloth; and applying tape to the sample followed by peeling it off. Dipping in water and MEK had no effect. Dipping in  $H_2SO_4$  removed both

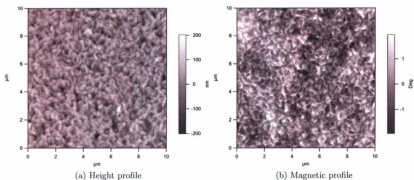


Figure 3.10: MFM image of untemplated cobalt, sample 191. Cobalt electrodeposited onto ITO substrate.  $-1.25$  V vs. SCE;  $1.500$  C of charge deposited.

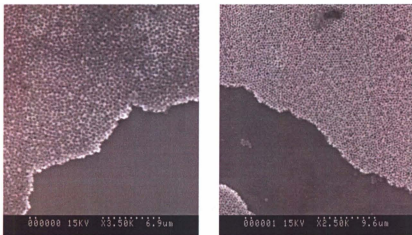


Figure 3.11: SEM images showing cobalt deposit peeling off with spheres. The regions of bare substrate indicates that all the material, both silica and cobalt, was removed. Sample 173:  $0.5$   $\mu\text{m}$  spheres spin-coated on an ITO substrate. Electrodeposit of cobalt at  $-1.25$  V vs. SCE;  $1.442$  C of charge deposited.

spheres and cobalt. Ultrasonication in water had little to no effect, and ultrasonication in NaOH appeared to remove the cobalt but not the spheres (the cobalt deposit for this sample was very thin). Wiping the sample tended to remove everything. Using scotch tape left a residue but did not remove the spheres.

### 3.6 Magnetic Simulations

Simulations of thin cobalt films were carried out using the commercial software package *LLG Micromagnetics*.<sup>15</sup> The modeled films were 640 nm  $\times$  320 nm in the  $xy$ -plane and from 10 nm to 50 nm thick. Cubic cells were 10 nm on a side; thus the films consisted of 64  $\times$  32 cells. For masked films, circular regions 160 nm in diameter were removed from the films (note that this is smaller than the 500 nm and 250 nm voids in the real samples). These holes were aligned to a square grid. In a 640 nm  $\times$  320 nm film there were therefore eight holes. Periodic boundary conditions were used in the  $xy$ -plane. The anisotropic easy axes of the cells were uniformly randomized to simulate the polycrystalline structure of the deposits seen under AFM. Parameters chosen were:  $K = 4 \times 10^6$  erg/cm<sup>3</sup> for the anisotropy magnitude;  $M_s = 1414$  emu/cm<sup>3</sup> for the saturation moment; and  $A = 3.05$   $\mu$ erg/cm for the exchange constant. Gaussian distributions of the anisotropy magnitude  $K$  and saturation moment  $M_s$  were also made by assigning standard deviations of 5% ( $\sigma_K = \sigma_M = 0.05$ , unless indicated otherwise). These settings represented a tradeoff between accuracy and reasonable computation time (computation time took anywhere from a thirty minutes to two days on a desktop PC, depending on the thickness and type of simulation). The limiting factor is the cell size: cells cannot be larger than 10 nm in order to ensure that uniformly magnetized cells are a good approximation. When cells are too large there is a greater chance of seeing an unphysical 180° flip between neighboring cells.<sup>16</sup> This small cell size limits the size of samples that can be reasonably simulated. The dimensions chosen were on the same order of magnitude as those in the samples, but small enough that calculation times were reasonable. Also note that in order to have periodic boundary conditions side lengths must be a power of two in the number of cells so that Fast Fourier Transform techniques can be used in the software.<sup>16</sup>

The main goal was to examine trends in the hysteresis loops which could be compared to similar trends in the samples. In addition to comparing masked and unmasked films, thickness was varied to examine its effect.

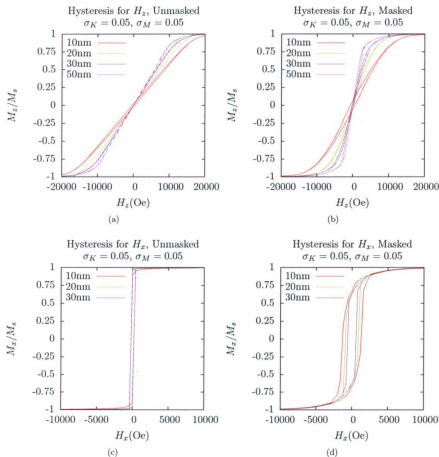


Figure 3.12: Hysteresis loops, various thicknesses. (a) Field applied perpendicular to the the plane of the film, no mask. (b) Field applied perpendicular to the plane of the film, masked. (c) Field applied parallel to the plane of the film, no mask. (d) Field applied parallel to the plane of the film, masked.

Figure 3.12 shows hysteresis loops with the applied field along either the  $z$  or  $x$

axis (perpendicular or in-plane, respectively). Loops (a) and (c) are plain films with no template, while (b) and (d) are masked films. The most obvious trend is that the  $z$  axis loops show increasing susceptibility (more squareness) with increasing thickness. Magnetostatic interactions favour having the magnetization parallel to the surface as this reduces demagnetizing fields and their associated energy cost. This is known as shape anisotropy, and the effect is greater in thinner films where a greater proportion of the magnetization is near the surface. Shape anisotropy also accounts for the difference in susceptibility between the  $z$  and  $x$  axis loops. Again, since thin films favour in-plane magnetization the sample will magnetize more easily along the  $x$  axis.

More interesting is the difference between the masked and unmasked films. Table 3.1 shows the data for the coercive fields ( $H_c$ ) obtained from the loops shown in Figure 3.12. As can be seen in the table, the masked films show greater coercive fields. To explain the difference in coercivity, recall that magnetization reversal occurs due to either domain wall motion or domain rotation, with domain wall motion being the easier of the two. The existence of the template isolates sections of the film into smaller regions. Domain walls cannot move through the empty spaces between these regions and thus the template makes magnetization reversal more difficult, and hence the coercivity is higher.

The masked films also show a higher squareness in the  $z$  axis loops. The larger slope may be explained by noting that the energy saved from having the magnetization lie in plane in a thin film (due to the reduced demagnetizing fields) is lessened by the presence of the openings in the material. These openings introduce surfaces that are not parallel to the substrate, and demagnetizing fields will cross the resulting gaps (see Figure 3.13). Lower energy savings lessens the resistance to the magnetization pointing out of plane and is therefore another form of shape anisotropy.

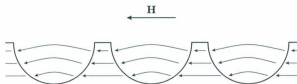


Figure 3.13: Demagnetizing fields crossing the gaps in the magnetic template when the external field is parallel to the surface.

Film	$H_c$ (Oe)		
	Masked	Unmasked	
10 nm	619	370	
$z$ axis	20 nm	240	10
	30 nm	139	*
10 nm	1297	194	
$x$ axis	20 nm	903	198
	30 nm	580	199

Table 3.1: Simulated coercive fields,  $\sigma_K = 0.05$ ,  $\sigma_M = 0.05$ . Results calculated by linear interpolation of data points crossing the zero magnetization axis, averaged from both crossings. \* indicates an unphysical result.

To test for the causes of these differences, additional simulations were carried out. In one test, the magnetostatic interaction was turned off, while in the other the exchange interaction was turned off. Care must be taken in interpreting these results, since removing these interactions is highly unrealistic. In order to test the explanations given, we are concerned with three questions:

- Do the  $x$  and  $z$  axis loops look the same in the absence of magnetostatic interactions?
- Is the difference in coercivity between masked and unmasked films reduced in the absence of the exchange interaction?
- Is the squareness similar between the masked and unmasked films in the absence of the magnetostatic interaction?

Figures 3.14 (a) and (b) show simulations with the magnetostatic interaction turned off for both cases of the field along  $z$  and  $x$  axes. Notice that the two results are virtually

identical. This is expected since the exchange interaction is isotropic and the easy axes are uniformly distributed. Thus there is no reason to expect any difference between the two loops in the absence of shape anisotropy. Therefore, differences seen between Figures 3.12 (a) and (c) (as well as (b) and (d)) are indeed due to shape anisotropy from magnetostatic interactions.

Figures 3.15 (a) and (b) show simulations with the exchange interaction turned off for both masked and unmasked films. Although not identical, it can be seen that the coercivities of masked and unmasked samples are very similar, especially in comparison to the differences seen in Figure 3.12. This implies a connection between the coercivity and the exchange interaction as suggested previously.

As to the last question (the similarity between masked and unmasked films in the absence of the magnetostatic interaction), refer back to Figure 3.14 (a) (or the nearly identical (b)). Note that there is very little difference in squareness between the loops of the masked and unmasked films. This implies that the differences in squareness seen in Figure 3.12 are primarily due to magnetostatic interactions which are altered by the absence of magnetic material.

### 3.7 Hysteresis Loop Measurements

Several samples were sent to Professor Johan van Lierop's nanomagnetism research group at the University of Manitoba for further analysis. Measurements of hysteresis loops were made using a Quantum Designs Magnetic Property Measurement System, a SQUID (Superconducting Quantum Interference Device) magnetometer. The hysteresis loops for temperatures at 10 K and 300 K are shown in Figure 3.16.  $\mathbf{H}$  is parallel to the plane of the film in all loops (this corresponds to  $x$  axis loops in the simulations). From this

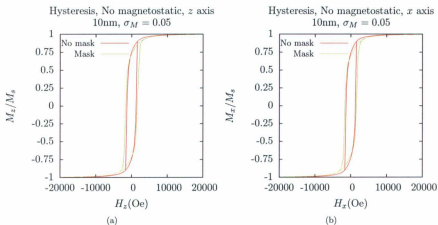


Figure 3.14: Hysteresis loops with magnetostatic interactions turned off. (a) Field perpendicular to the plane of the film. (b) Field parallel to the plane of the film.

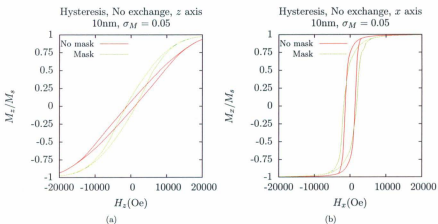


Figure 3.15: Hysteresis loops with the exchange interaction turned off. (a) Field perpendicular to the plane of the film. (b) Field parallel to the plane of the film.

data the values of the coercive fields were obtained for each sample at both temperatures.

These values are reported in Table 3.2.

As discussed in Section 3.6, in magnetic simulations it was found that masked samples

Sample	Type	Spheres	Charge Passed (C)	$H_c$ (Oe)	
				10 K	300 K
182	Masked	0.50 $\mu\text{m}$	1.499	470	126
183	Masked	0.25 $\mu\text{m}$	0.500	789	245
188	Masked	0.25 $\mu\text{m}$	1.000	880	255
189	Unmasked	None	1.000	508	147

Table 3.2: Experimental coercive fields, various samples. Results calculated by linear interpolation of data points crossing the zero magnetization axis, averaged from both crossings.

had a higher coercivity than unmasked samples. As can be seen in Table 3.2, this holds true experimentally as well (e.g. samples 183 and 188, being masked, have greater coercive fields than sample 189, which has no mask). Similar increases in coercivity in templates such as these have been reported.<sup>33-35</sup> One sample (182) does not follow this trend – despite being a masked sample its coercivity is comparable to that of an unmasked sample (189). This might be related to the larger sphere diameter relative to the other templated samples measured, or to the presence of gaps in the template (see Figure 3.7). Recall from Section 3.6 that the proposed explanation for the increase in coercivity was the template halting domain wall motion. Large gaps in the template could prevent this effect. As another possibility, Zhukov *et al.* have noted<sup>36</sup> an oscillatory dependence of the coercivity based on the thickness of antidot arrays such as these, with the coercivity peaking when the thickness is half the diameter of the voids. They attribute this effect to domain wall pinning. If the coercivity of samples is thickness dependant then it could be that the thickness of sample 182 is between peaks and the coercivity is therefore lower. This effect would not have been noticed in our simulations in which cylindrical voids were used.

Our samples show no significant difference in squareness between masked and unmasked films. However, the previously noted difference in the simulations was between masked and unmasked films when  $\mathbf{H}$  was perpendicular to the plane of the film, while in these measurements  $\mathbf{H}$  is in plane. A comparison between simulation and experiment

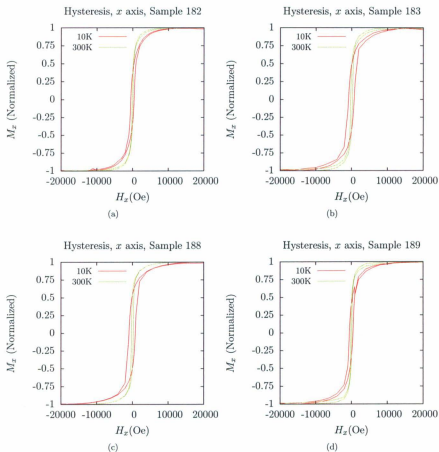


Figure 3.16: Experimentally determined hysteresis loops (Johan van Lierop, University of Manitoba). (a) Sample 182: Masked,  $0.50 \mu\text{m}$  spheres,  $1.499 \text{ C}$ . (b) Sample 183: Masked,  $0.25 \mu\text{m}$  spheres,  $0.500 \text{ C}$ . (c) Sample 188: Masked,  $0.25 \mu\text{m}$  spheres,  $1.000 \text{ C}$ . (d) Sample 189: No mask,  $1.000 \text{ C}$ .

along these lines is therefore not possible with this data.

## Chapter 4

# Conclusions

The primary focus of this thesis is on the production, characterization and simulation of patterned magnetic films. Much of the work was focused on techniques producing consistent patterned magnetic samples by using spin-coated colloidal spheres as templates. MFM analyses reveal the presence of magnetic structures in the resulting samples. However, quantifying magnetic domain structure is difficult while the templating spheres remain in place. Magnetic simulations revealed interesting differences in the coercivity and squareness between patterned and unpatterned films, and experimental data showed some similarities in the coercivity, but the data set is too small to make firm conclusions. In order to better understand these comparisons, future work will need to focus on removal of the spheres and obtaining more hysteresis loops of the samples.

A scheme to produce consistent magnetic templates was developed using spin-coated colloidal spheres and electrodeposition. A colloidal suspension consisting of 500 nm or 250 nm spheres was spin-coated onto the substrate. This produced a single layer of spheres. Cobalt was then deposited through these spheres using a solution of cobalt sulphate and boric acid. In order to obtain samples of sufficient thickness, between 1 C and 1.5 C

of charge must be deposited (over an area of approximately  $2.5 \text{ cm}^2$ ). Methods using vapour deposition were tried, however complications resulted in thin deposits and a lack of control over the thickness.

These samples were examined using SEM, AFM, MFM and (for some) a SQUID magnetometer. Cobalt was deposited in sufficient quantity to be clearly visible under SEM, and magnetic structures were clearly seen with MFM. These studies show that the colloidal sphere template is polycrystalline. Unfortunately, the presence of the spheres inhibited the quantitative assessment of the magnetic structures within the samples. Control of the adherence of the colloidal film to the substrate is a complex problem. Studying techniques for removing the colloidal spheres would be important for any future projects.

Simulations were carried out to investigate the effects of patterning thin films. These simulations show that patterned films have greater coercive fields and squareness as compared to unpatterned films. Additional simulations show that the greater squareness is due to changes in the magnetostatic interaction, and that the greater coercivity is likely due to voids restricting domain wall movement. Hysteresis loops obtained with a magnetometer partially confirmed the trend of patterned films showing greater coercivity. To obtain more conclusive results, more measurements will need to be taken. Also interesting would be a study of the crystal properties of the electrodeposited cobalt. While AFM and MFM images of unpatterned samples give some clues about the crystal structure of the deposits, quantitative data would be more useful. There is also no guarantee that deposits in the presence of a template will be the same as those in the absence of one. Although x-ray diffraction measurements were taken, the signal to noise ratio was not high enough to resolve the crystal structure. Simulations were carried out assuming uniformly

randomized crystal orientations (and therefore uniformly randomized easy axes). Better knowledge of the crystal orientation could improve the accuracy of the simulations.

In this thesis we have demonstrated a feasible method to produce patterned magnetic materials using self-assembly of colloidal spheres. These patterned magnetic films have potential applications in magnetic storage media. The methods involved take place at room temperature and atmospheric pressure which simplifies the manufacturing process. Additionally, we have compared theoretical predictions of the behaviour of these systems (*via* simulations) with experimental results, and found them to be in general agreement.

## Appendix A

### Samples Prepared

The following tables record sample preparation conditions and notes. Table A.1 contains samples that were spin-coated with silica spheres, but on which no magnetic material was deposited. Table A.2 contains samples which were coated using vapour deposition. Note that vapour deposition allows several samples to be coated at once. The relevant parameters are indicated for all samples in a batch. Tables A.3 and A.4 contain samples coated using electrodeposition.

Sample	Sphere Size	MEK/Silica Ratio (ml/g)	RPM	MFM/AFM Images	SEM Images	Notes
43	0.50	3.584	2000	3		
44	0.50	3.584	2200	7		
45	0.50	3.584	2400	3		Dipped in H <sub>2</sub> O and wiped. Some spheres removed.
46	0.50	3.584	2600			Dipped in H <sub>2</sub> O and dried in air. No spheres removed.
47	0.50	3.584	2800			Wiped with dry cloth. Most spheres removed.
48	0.50	3.584	3000	1		Rubbed with cloth soaked in MEK. Most spheres removed.
49	0.50	3.584	3200	1		Dipped in H <sub>2</sub> O for about 5 minutes. No spheres removed.
50	0.50	3.584	3400			Dipped in MEK for about 5 minutes. No spheres removed.
51	0.50	3.584	3600	5		Dipped in MEK and dried in air. No spheres removed.
52	0.50	3.584	3800			Dipped in MEK and wiped. Some spheres removed.
53	0.50	3.584	2200	2		
54	0.50	3.584	2600	1		Unaccounted for
55	0.50	3.584	3000	4		
56	0.50	3.584	3400	1		
57	0.50	3.584	3800	1		
58	0.50	5.375	2000			
59	0.50	5.375	2500		5	
60	0.50	5.375	3000			Unaccounted for
61	0.50	5.375	3500		4	
62	0.50	5.375	4000			Unaccounted for
63	0.50	7.167	3000			
100	0.10	7.167	3000	2		
101-115	0.10	7.167	3000			
116-131	0.25	7.167	3000			
132-146	0.50	7.167	3000			
147	0.50	7.167	3000	1		

Table A.1: Spin coating samples. All samples made with glass slide substrate and 37  $\mu$ L of solvent.

Sample	Sphere Size	Solvent Volume ( $\mu$ L)	Cobalt Deposited?	Copper Deposited?	All Deposited?	MFM/AFM Images	SEM Images	Notes
64	0.50							
65	0.50						18	One end ultrasonicated for 15s in NaOH. Cobalt removed, spheres remain. Other end 15s in H <sub>2</sub> O, spheres and cobalt removed. Center wiped with cloth, both removed.
66	0.50		Unknown amount	0 g	N/A	2		
67	0.50							
68	0.50							
69	0.50							
70	0.50						10	Ultrasonicated for 15s in NaOH. Cobalt removed spheres remain.
77	0.25	30						
78	0.25	30				2		Appears to be a monolayer
79	0.25	40						
80	0.25	45						
81	0.50	37	0.4384 g	No	No	1		Appears to be a bilayer
82	0.50	37						
83	0.50	37						
84	0.50	37				2		

Table A.2: Vapor deposited samples. Samples made in two batches, 64-70 and 77-84. All spin coated samples made with solvent at a concentration of 7.167 mL/g MEK to silica dropped on to a glass substrate spun at 3000 RPM.

Sample	Substrate	Sphere Size	Voltage (V)	Current (mA)	Time (mm:ss)	Charge (C)	MFM/AFM Images	SEM Images	Notes
29			-1.25		2:00				
71	ITO Coverslip	0.50	-1.25	-	-	-			Wrong side of ITO facing up, no electrodeposit
72	ITO Coverslip	0.50	-1.25	-	0:05	-		7	Attempted sphere removal, 2 minutes in H <sub>2</sub> O ultrasonication
73	ITO Coverslip	0.50	-1.25	-	-	-			Wrong side of ITO facing up, no electrodeposit
74	ITO Coverslip	0.50	-1.25	-	-	-			Wrong side of ITO facing up, no electrodeposit
75	ITO Coverslip	0.50	-1.25	-	0:30	-	16	13	Attempted sphere removal, 15 seconds in H <sub>2</sub> O ultrasonication
76	ITO Coverslip	0.50	-1.25	-	0:15	-	20	11	Attempted sphere removal, 30 seconds in dilute NaOH ultrasonication
148	ITO Coverslip	0.25	-1.25	-	2:00	-			
149	ITO Coverslip	0.25	-1.25	-	2:00	-	4		
150	ITO Coverslip	0.25	-1.25	-	3:00	-	2		
151	ITO Coverslip	0.25	-1.25	-	-	-			
152	ITO Coverslip	0.25	-1.25	-	1:00	-			
153	ITO Coverslip	0.25	-1.25	-2.0	0:30	-			
154	ITO Coverslip	0.25	-1.20	-1.0	3:00	-	4		No sphere coating
155	ITO Coverslip	0.25	-	-	-	-			No sphere coating
156	ITO Coverslip	0.25	-	-	-	-			Spheres came off in H <sub>2</sub> SO <sub>4</sub> dip
157	ITO Coverslip	0.25	-	-	-	-			Spheres came off in H <sub>2</sub> SO <sub>4</sub> dip
158	ITO Coverslip	0.25	-1.12	-2.0	2:00	-			Spheres came off in H <sub>2</sub> SO <sub>4</sub> dip
159	ITO Coverslip	0.25	-	-	-	-			Cobalt deposit came off in H <sub>2</sub> SO <sub>4</sub> dip
160	ITO Coverslip	0.50	-1.20	-0.4	50:00	-	3		Spheres came off in H <sub>2</sub> SO <sub>4</sub> dip
161	ITO Coverslip	0.50	-1.25	-3.5	1:30	-	6		Spheres came off in H <sub>2</sub> SO <sub>4</sub> dip in some regions prior to deposit
162	ITO Coverslip	0.50	-1.20	-3.0	1:30	-			Unaccounted for
163	ITO Coverslip	0.50	-	-	-	-			Unaccounted for
164	ITO Coverslip	0.50	-	-	-	-			Unaccounted for

Table A.3: Electrodeposition samples. All spin coated samples made with 37  $\mu\text{L}$  of solvent at a concentration of 7.167 mL/g MEK to silica dropped on to a substrate spun at 3000 RPM.

Sample	Substrate	Sphere Size	Voltage (V)	Current (mA)	Time (min:sec)	Charge (C)	MFM/AFM Images	SEM Images	Notes
165	ITO Coverslip	0.50	-1.10	-4.0	3:00		3		
166	ITO Coverslip	0.50	-1.20	-3.5	3:00				
167	ITO Coverslip	0.50	-1.25	-2.5	3:00		3		
168	ITO Coverslip	0.50	-1.25	-4.0	10:00		2		Flake of 168 Flake of 168
169									
170	ITO Slide 70-100 Ω	0.50	-1.25	-3.0	7:30		3	42	
171	ITO Slide 70-100 Ω	0.50	-1.25	-2.8	10:00		9	55	
172	ITO Slide 70-100 Ω	0.50	-1.25	-3.5	8:00	1.442		24	Charge measurement restarted after 30 seconds
173	ITO Slide 70-100 Ω	0.50	-1.25	-3.1	7:00	1.376		15	
174	ITO Slide 70-100 Ω	0.50	-1.25	-4.0	6:42	1.715			No sphere coating
175	ITO Slide 70-100 Ω	0.50	-1.25	-3.3	7:00	1.339		2	Shard of 176
176	ITO Slide 70-100 Ω	0.50	-1.25	-3.5	4:35	0.999	9		No sphere coating
177	ITO Slide 70-100 Ω	0.50	-1.25	-3.0	5:11	1.000			CV graph from deposit missing
180	ITO Slide 70-100 Ω	0.50	-1.25	-3.0	6:01	1.249	3		Broken into pieces
181	ITO Slide 70-100 Ω	0.50	-1.25	-3.0	8:04	1.499	3		
182	ITO Slide 70-100 Ω	0.50	-1.25	-3.0					Time not recorded. Charge counting started several seconds late.
183	ITO Slide 70-100 Ω	0.25	-1.25	-3.0		0.500			Electrolyte dirty, coverage uneven. Dropped on floor. No electrodeposit
184	ITO Slide 70-100 Ω	0.25	-1.25	-3.0	3:26	0.626			
185	ITO Slide 70-100 Ω	0.25	-	-	-	-			
186	ITO Slide 30-60 Ω	0.25	-1.25	-4.5	2:12	0.600			Titled with respect to counter electrode, coverage uneven
187	ITO Slide 30-60 Ω	0.25	-1.25	-5.0	3:30	0.800	3		Deposit time approximate
188	ITO Slide 30-60 Ω	0.25	-1.25	-5.0	3:59	1.000	6		No sphere coating
189	ITO Slide 30-60 Ω	-	-1.25	-4.0	4:29	1.251			No sphere coating
190	ITO Slide 30-60 Ω	-	-1.25	-5.0	4:29	1.251			No sphere coating. Most of electrodeposit washed off.
191	ITO Slide 30-60 Ω	-	-1.25	-4.5	5:26	1.500	7		

Table A.4: Electrodeposition samples. All spin coated samples made with 37 μL of solvent at a concentration of 7.167 mL/g MEK to silica dropped on to a substrate spun at 3000 RPM.

## Appendix B

### Additional Sample Images

The following are additional images of selected samples not shown in the main text.

#### B.1 Samples With Spheres

The following are samples made by spin-coating spheres followed by electrodepositing cobalt.

##### B.1.1 Sample 168

###### Preparation Conditions

0.5  $\mu\text{m}$  spheres were mixed with MEK at a ratio of 7.167 mL/g. Suspension spin-coated at 3000 RPM on an ITO substrate. Electrodeposit of cobalt at  $-1.25$  V vs. SCE for 10:00.

## Cobalt Growth Between spheres

The following images show parts of the sample where cobalt was present between the spheres.

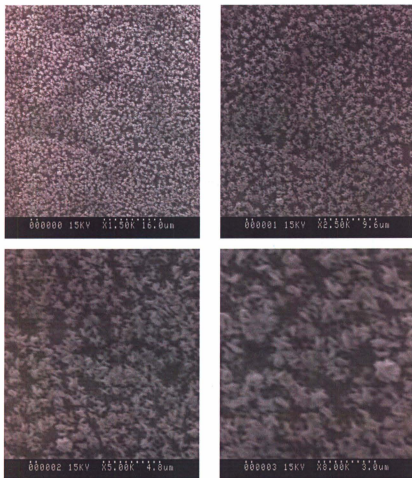


Figure B.1: Sample 168, cobalt growth between the spheres

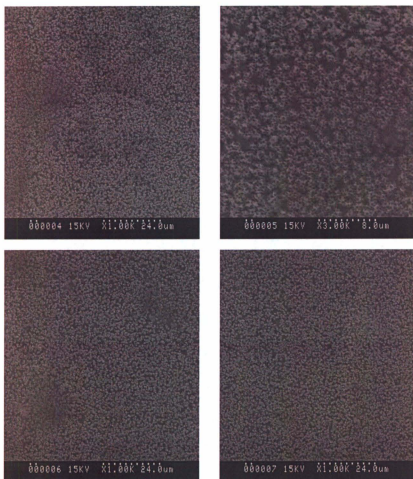


Figure B.2: Sample 168, cobalt growth between the spheres

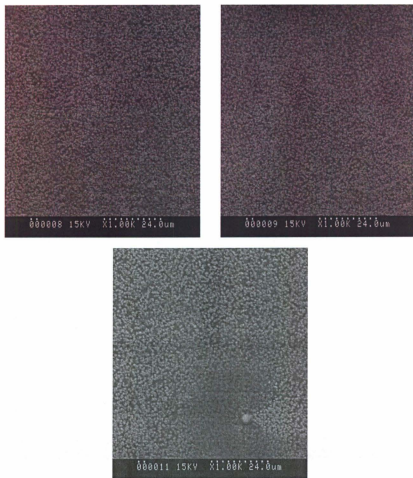


Figure B.3: Sample 168, cobalt growth between the spheres

## Cobalt Growth Over Spheres

The following images show parts of the sample where cobalt grew over the spheres entirely.

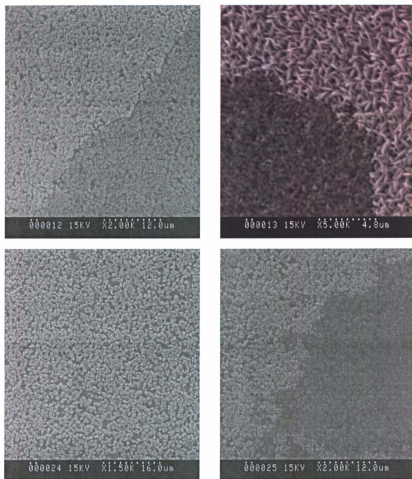


Figure B.4: Sample 168, parts of the sample where cobalt has grown over the spheres entirely

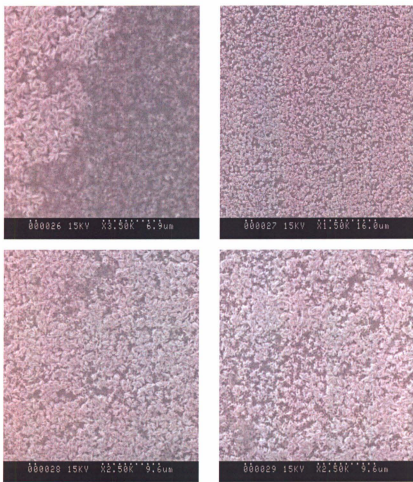


Figure B.5: Sample 168, parts of the sample where cobalt has grown over the spheres entirely

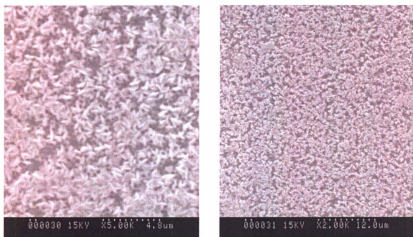


Figure B.6: Sample 168, parts of the sample where cobalt has grown over the spheres entirely

### Increasing Cobalt Density

The following series of images follows a straight line from a region which was not submerged in electrolyte during the electrodeposit (and therefore has no cobalt present) to one which was, covering a range of 2.25 mm. The cobalt density increases gradually.

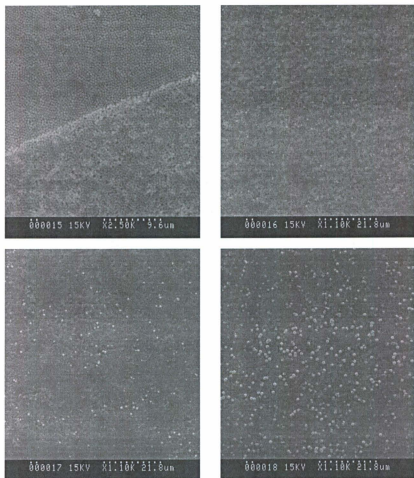


Figure B.7: Sample 168, Showing the cobalt density increasing, starting from a region which was not submerged in electrolyte during the electrodeposit, and moving towards one which was.

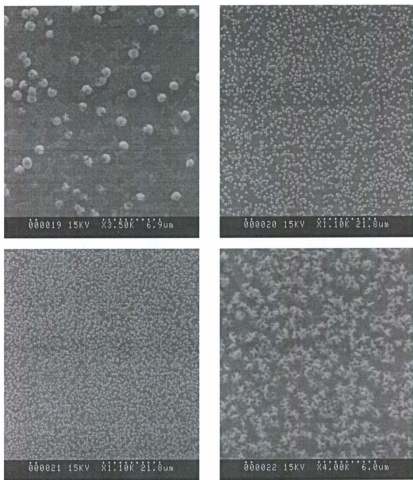


Figure B.8: Sample 168, continuation of the series depicted in Figure B.7

### Cobalt Peeling Off

The following images show regions where the cobalt has peeled off, taking most the spheres with it.

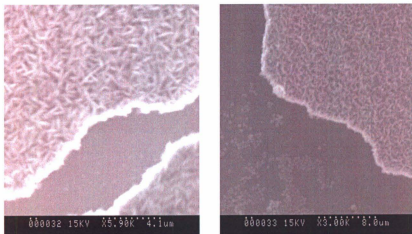


Figure B.9: Sample 168, cobalt deposit peeling off

## B.1.2 Sample 172

### Preparation Conditions

0.5  $\mu\text{m}$  spheres were mixed with MEK at a ratio of 7.167 mL/g. Suspension spin-coated at 3000 RPM on an ITO substrate. Electrodeposit of cobalt at  $-1.25$  V vs. SCE for 10:00.

### Cobalt Growth Between spheres

The following images show parts of the sample where cobalt was present between the spheres.

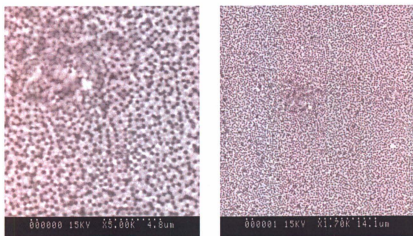


Figure B.10: Sample 172, cobalt growth between the spheres

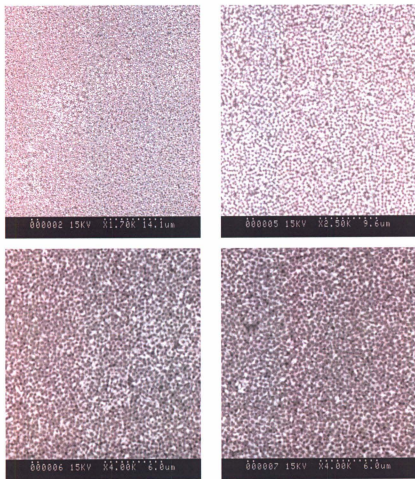


Figure B.11: Sample 172, cobalt growth between the spheres

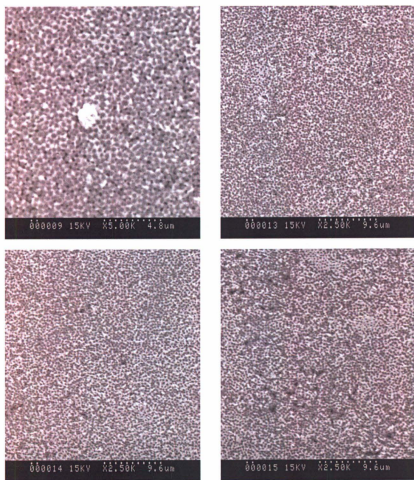


Figure B.12: Sample 172, cobalt growth between the spheres

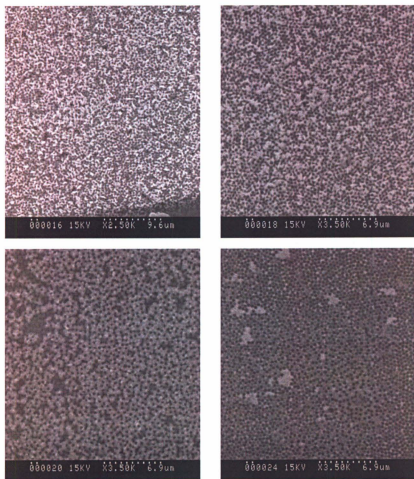


Figure B.13: Sample 172, cobalt growth between the spheres

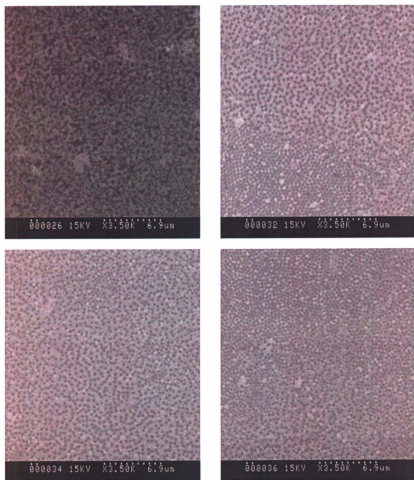


Figure B.14: Sample 172, cobalt growth between the spheres

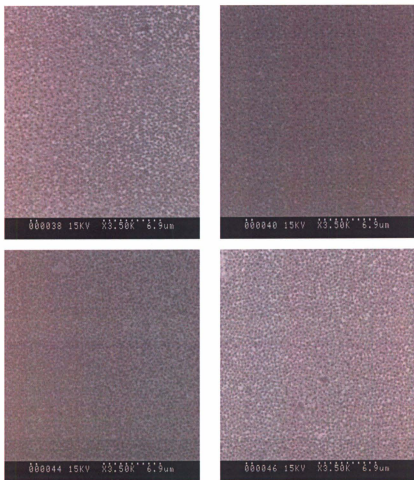


Figure B.15: Sample 172, cobalt growth between the spheres

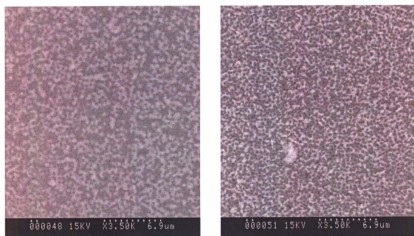


Figure B.16: Sample 172, cobalt growth between the spheres

## Cobalt Growth Over Spheres

The following images show parts of the sample where cobalt grew over the spheres entirely.

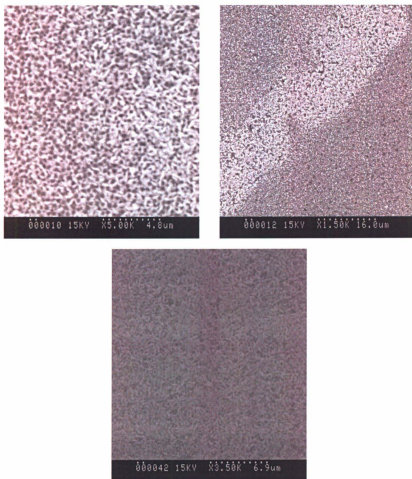


Figure B.17: Sample 172, parts of the sample where cobalt has grown over the spheres entirely

## MFM Images

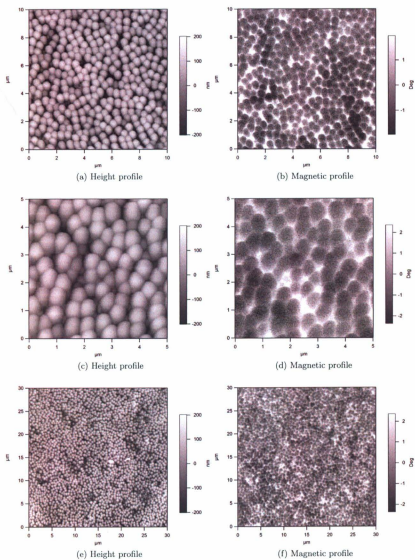


Figure B.18: Sample 172, additional MFM images depicting magnetic structure

### B.1.3 Sample 173

#### Preparation Conditions

0.5  $\mu\text{m}$  spheres were mixed with MEK at a ratio of 7.167 mL/g. Suspension spin-coated at 3000 RPM on an ITO substrate. Electrodeposit of cobalt at  $-1.25$  V vs. SCE. 1.442 C of charge deposited.

#### Cobalt Growth Between spheres

The following images show parts of the sample where cobalt was present between the spheres.

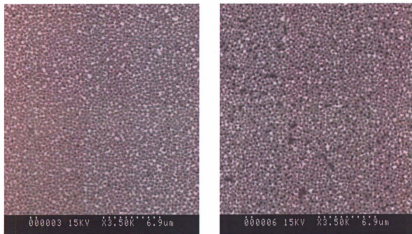


Figure B.19: Sample 173, cobalt growth between the spheres

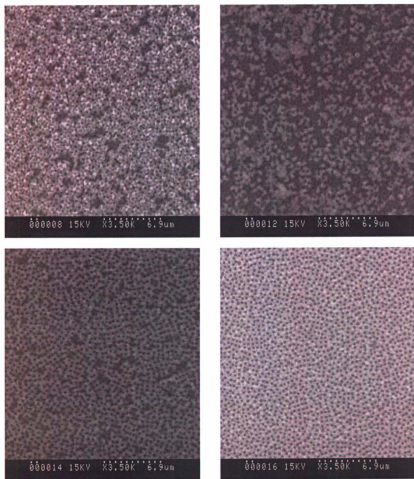


Figure B.20: Sample 173, cobalt growth between the spheres

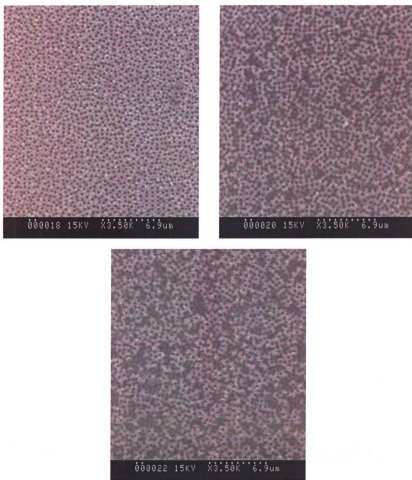


Figure B.21: Sample 173, cobalt growth between the spheres

### B.1.4 Sample 174

#### Preparation Conditions

0.5  $\mu\text{m}$  spheres were mixed with MEK at a ratio of 7.167 mL/g. Suspension spin-coated at 3000 RPM on an ITO substrate. Electrodeposit of cobalt at  $-1.25\text{ V vs. SCE}$ . 1.376 C of charge deposited.

#### Cobalt Growth Between spheres

The following images show parts of the sample where cobalt was present between the spheres.

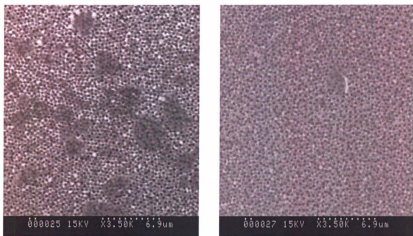


Figure B.22: Sample 174, cobalt growth between the spheres

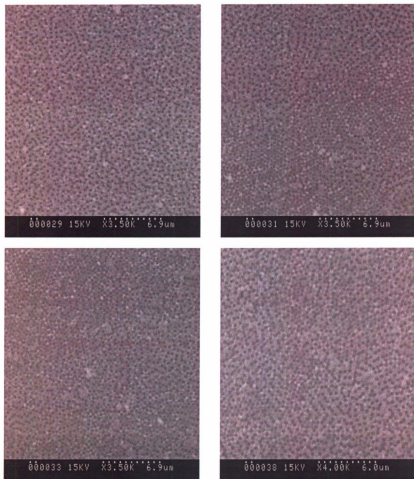


Figure B.23: Sample 174, cobalt growth between the spheres

## B.2 Samples Without Spheres

The following are samples with a cobalt electrodeposit but no spheres.

### B.2.1 Sample 179

#### Preparation Conditions

Cobalt electrodeposited onto ITO substrate at  $-1.25$  V vs. SCE.  $0.999$  C of charge deposited.

## MFM Images

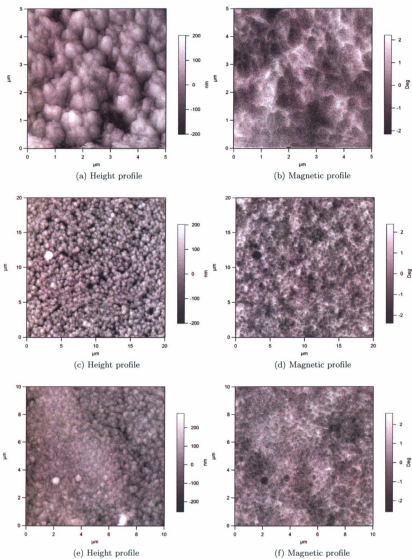


Figure B.24: Sample 179, additional MFM images depicting magnetic structure

## B.2.2 Sample 189

### Preparation Conditions

Cobalt electrodeposited onto ITO substrate at  $-1.25$  V vs. SCE. 1.000 C of charge deposited.

### MPM Images

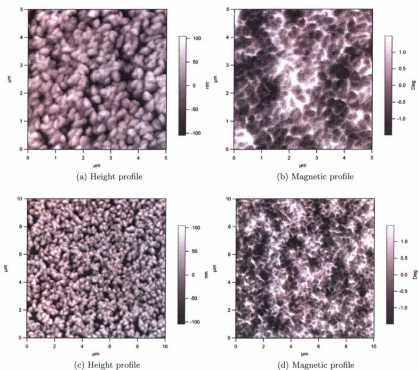


Figure B.25: Sample 189, additional MPM images depicting magnetic structure

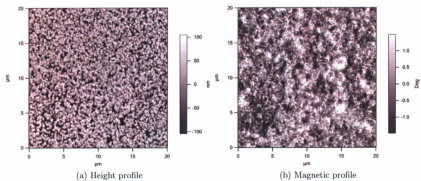


Figure B.26: Sample 189, additional MFM images depicting magnetic structure

### B.2.3 Sample 191

#### Preparation Conditions

Cobalt electrodeposited onto ITO substrate at  $-1.25$  V vs. SCE. 1.500 C of charge deposited.

#### MFM Images

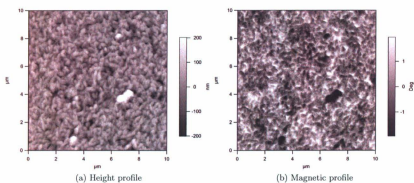


Figure B.27: Sample 191, additional MFM images depicting magnetic structure

## Bibliography

- [1] B. D. Terris. Fabrication challenges for patterned recording media. *Journal of Magnetism and Magnetic Materials*, 321:512–517, 2009.
- [2] B. Terris, T. Thomson, and G. Hu. Patterned media for future magnetic data storage. *Microsystem Technologies*, 13:189–196, 2007.
- [3] Y. Shiroishi, K. Fukuda, I. Tagawa, H. Iwasaki, S. Takenoiri, H. Tanaka, H. Mutoh, and N. Yoshikawa. Future options for HDD storage. *IEEE Transactions on Magnetics*, 45(10):3816–3822, 2009.
- [4] B. D. Terris and T. Thomson. Nanofabricated and self-assembled magnetic structures as data storage media. *Journal of Physics D: Applied Physics*, 38, 2005.
- [5] P. N. Bartlett. Electrodeposition of nanostructured films using self-organizing templates. *The Electrochemistry Society Interface*, 13(4):28–33, 2004.
- [6] T. Ito and S. Okazaki. Pushing the limits of lithography. *Nature*, 406:1027–1031, 2000.
- [7] R. A. L. Jones. *Soft Condensed Matter*. Oxford University Press Inc., New York, 2002.

- [8] N. J. Wagner and J. F. Brady. Shear thickening in colloidal dispersions. *Physics Today*, 62(10):27–32, 2009.
- [9] D. J. Norris, E. G. Arlinghaus, L. Meng, R. Heiny, and L. E. Scriven. Opaline photonic crystals: How does self-assembly work? *Advanced Materials*, 16(16):1393–1399, 2004.
- [10] A. Mihi, M. Ocaña, and H. Míguez. Oriented colloidal-crystal thin films by spin-coating microspheres dispersed in volatile media. *Advanced Materials*, 18:22442249, 2006.
- [11] P. Jiang and M. J. McFarland. Large-scale fabrication of wafer-size colloidal crystals, macroporous polymers and nanocomposites by spin-coating. *Journal of the American Chemical Society*, 126:13778–13786, 2004.
- [12] C. Acros, K. Kumar, W. González-Viñas, R. Sirera, K. M. Poduska, and A. Yethiraj. Orientationally correlated colloidal polycrystals without long range positional order. *Physical Review E*, 77(5):050402, 2008.
- [13] S. Blundell. *Magnetism in Condensed Matter*. Oxford University Press Inc., New York, 2001.
- [14] B. D. Cullity. *Introduction to Magnetic Materials*. Addison-Wesley Publishing Company, Inc., 1972.
- [15] LLG Micromagnetics Simulator website. <http://llgmicro.home.mindspring.com/>.
- [16] M. R. Scheinfein and E. A. Price. *LLG User Manual v2.50*. 1997.
- [17] M. d’Aquino. *Nonlinear Magnetization Dynamics in Thin-Films and Nanoparticles*. PhD thesis, University of Naples “Federico II”, 2004.

- [18] C. Kittel. *Introduction to Solid State Physics*. John Wiley & Sons, Inc., New Jersey, eighth edition, 2005.
- [19] E. D. Dahlberg and J. Zhu. Micromagnetic microscopy and modeling. *Physics Today*, 48(4):34–40, 1995.
- [20] T. L. Gilbert. A phenomenological theory of damping in ferromagnetic materials. *IEEE Transactions on Magnetics*, 40(6):3443–3449, 2004.
- [21] M. Plumer, J. van Ek, and D. Weller. *The Physics of Ultra-High-Density Magnetic Recording*. Springer-Verlag, 2001.
- [22] L. Landau and E. Lifshitz. On the theory of the dispersion of magnetic permeability in ferromagnetic bodies. *Phys. Zeitsch. der Sow*, 8:153–169, 1935.
- [23] S. Nakahara and S. Mahajan. The influence of solution pH on microstructure of electrodeposited cobalt. *Journal of the Electrochemical Society*, 127(2):283–288, 1980.
- [24] J. Goddard and J. G. Wright. The effect of solution pH and applied magnetic field on the electrodeposition of thin single-crystal films of cobalt. *British Journal of Applied Physics*, 15(7):807–814, 1964.
- [25] M. Bhuiyan, B. Taylor, M. Paranthaman, J. Thompson, and J. Sinclair. Microstructure and magnetic properties of electrodeposited cobalt films. *Journal of Materials Science*, 2008.
- [26] D. R. Cliffe and J. P. G. Farr. Growth habits of electrodeposited nickel and cobalt. *Journal of The Electrochemical Society*, 111(3):299–306, 1964.
- [27] J.L. Bubendorff, C. Mny, E. Beaurepaire, P. Panissod, and J.P. Bucher. Electrodeposited cobalt films: hcp versus fcc nanostructuring and magnetic properties. *The*

*European Physical Journal B - Condensed Matter and Complex Systems*, 17(4):635–643, 2000.

- [28] A. J. Bard and L. R. Faulkner. *Electrochemical Methods: Fundamentals and Applications*. John Wiley & Sons, Inc., New York, 2001.
- [29] D. Pullini and D. Busquets-Mataix. Electrodeposition efficiency of Co and Cu in the fabrication of multilayer nanowires by polymeric track-etched templates. *ACS Applied Materials & Interfaces*, 3(3):759–764, 2011.
- [30] W. Benenson, J. W. Harris, H. Stocker, and H. Lutz. *Handbook of Physics*. Springer, New York, 2002.
- [31] D. Rugar, H. J. Mamin, P. Guethner, S. E. Lambert, J. E. Stern, I. McFadyen, and T. Yogi. Magnetic force microscopy: General principles and application to longitudinal recording media. *Journal of Applied Physics*, 68(3):1169–1183, 1990.
- [32] K. Kumar. Preparation and characterization of spin-coated colloidal templates and patterned electrodeposited cobalt. Master's thesis, Memorial University of Newfoundland, 2008.
- [33] P. N. Bartlett, M. A. Ghanem, I. S. El Hallag, P. de Groot, and A. Zhukov. Electrochemical deposition of macroporous magnetic networks using colloidal templates. *Journal of Materials Chemistry*, 13(10):2596–2602, 2003.
- [34] A. A. Zhukov, A. V. Goncharov, P. A. de Groot, P. N. Bartlett, and Mohamed A. G. Magnetic antidot arrays from self-assembly template methods. *Journal of Applied Physics*, 93(10):7322, 2003.

- [35] A. K. Srivastava, S. Madhavi, White T. J., and R. V. Ramanujan. Template assisted assembly of cobalt nanobowl arrays. *Journal of Materials Chemistry*, 15:4424–4428, 2005.
- [36] A. A. Zhukov, A. V. Goncharov, P. A. de Groot, Mohamed A. G., P. N. Bartlett, R. Boardman, H. Fangohr, V. Novosad, and G. Karapetrov. Oscillatory thickness dependence of the coercive field in magnetic three-dimensional antidot arrays. *Applied Physics Letters*, 88:062511, 2006.





